nature materials

SUPPLEMENTARY INFORMATION

DOI: 10.1038/NMAT4801

Localized dielectric breakdown and antireflection coating in metal–oxide–semiconductor photoelectrodes

Li Ji, Hsien-Yi Hsu, Xiaohan Li, Kai Huang, Ye Zhang, Jack C. Lee, Allen J. Bard and Edward T. Yu

Sections **Page**

DOI: 10.1038/NMAT4801

I. Materials and fabrication methods

Substrate preparation

Two types of 4 inch Si (001) wafers were used as substrates in this study. n-Si (phosphorus doped, ρ = 0.5-1 Ω cm) substrates were used for photoanodes and p-Si (boron doped, ρ = 1-5 Ω cm) for photocathodes. The Si wafers were first cleaved into 1cm×1cm square pieces, followed by cleaning with piranha solution (H_2O: H_2SO_4: H_2O_2), buffered oxide etch solution (BOE, HF: HCl: NH_4F) and deionized water (DI), in succession. The back contact was formed by e-beam evaporation of 5nmCr/100nmAu.

n-GaAs (100)-oriented (Te-doped, 1×10^{17} cm^{-3}) polished substrates were used for the GaAs-based photoanode. The wafers were cleaned by BOE, acetone, isopropyl alcohol (IPA), deionized water, in succession. The back contact was formed by e-beam evaporation of 10nmNi/50nm$Au_{88}Ge_{12}$.

Metal oxide growth

1. SiO_2

SiO_2 thin films were grown by three methods.

First, high quality thermal SiO_2 films were grown at 950 ºC in an oxidation furnace (MRL 8' furnace, Sandvik Thermal Process Inc) in dry O_2 ambient. This method has been widely used to fabricate gate oxides in MOSFETs with good interfacial quality and low defect density. The p or n-Si/SiO_2 samples shown in the main manuscript were all grown by this method.

Second, ebeam evaporation was used to deposit SiO_2 on Si substrates as a reference samples, in order to investigate the dependence of dielectric breakdown properties on the quality of metal oxides, as discussed in detail in *Section II.*

For structures in which GaAs was used for the photoanode, high quality silicon oxides were grown by plasma-enhanced-atomic-layer-deposition (PEALD) (*1-4*). In addition, before the deposition of SiO_2, a 1.5 nm thick Al_2O_3 was first grown by thermal ALD on the GaAs substrate to reduce the interfacial defect density and stabilized the substrate, a standard process developed by Ye *et. al. (5)*. The silicon oxide PEALD was performed in a Fiji ALD with remote plasma & ozone generator system (Cambridge Nanotech), with tris-dimethylamino-silane and plasma ozone as precursors. The growth temperature was 100 ºC and the growth rate was ~0.8 Å/cycle. Remote mode was used, in which the plasma sources were located remotely from the substrate stage to improve control of plasma properties.

2. TiO_2 and Al_2O_3

Thermal ALD of TiO_2 and Al_2O_3 have been widely studied. Here in this work, we used standard recipes, as described below, in a ALD SavannahTM 200 system (Cambridge NanoTech). The growth temperatures were all set to 200 ºC. For TiO_2, the pulse time for H_2O and tetrakistitanium were 0.015s and 0.1s, respectively. For Al_2O_3, the pulse time for H_2O and trimethyaluminum were 0.015s and 0.015s, respectively.

Metallization

Permalloy (Py) was used as the OER catalyst for all photoanodes and Ti/Pt bilayers were used as HER catalysts for all photocathodes. A series of standard photolithography, e-beam evaporation and lift-off processes were performed to pattern regular array structures on photoelectrodes with various pitch sizes. The thicknesses of Py and Ti/Pt were 150 nm and 30nm/20nm, respectively. AZ5209 was used as positive photoresist for photolithography and Remover PG (MicroChem) was used for lift-off. Then the samples were rinsed by acetone, IPA and DI water with ultrasonic agitation for 5 mins each.

II. Dielectric Breakdown

Brief theory of dielectric breakdown

Electrical breakdown of dielectric layers in metal-oxide-semiconductor devices has been studied for decades in the context of reliability and device failure, and more recently has been investigated for applications in non-volatile memory.

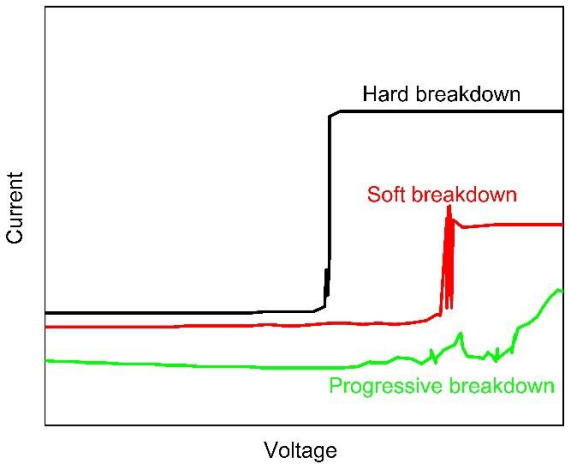

Fig. S1. Schematic of the three different kinds of breakdown occurrences by ramp voltage sweep**.**

There are different modes of breakdown that can occur in dielectric thin films, including hard breakdown (HBD), soft breakdown (SBD) and progressive breakdown (PBD)(*6-14*). Under electrical stressing at constant voltage, they show different behaviors as illustrated in Fig. S1. When soft or hard breakdown occurs, the current rapidly increases. The magnitude of current after breakdown distinguishes SBD from HBD, and the different current levels are attributed to a difference of conduction path created in the oxide by defect percolation. PBD does not show a sharp transient and typically only occurs in oxides thinner than ~25 Å. For the purpose of this work, high current after breakdown is desired, and we therefore attempt to induce HBD.

Much less is known about the post-breakdown conduction mechanism mainly because of the random nature of breakdown and sample-to-sample-variation. Several models have been proposed, such as junction-like conduction, variable-range hopping, direct tunneling and trap-assisted tunneling. Regarding the nature of the breakdown process, what is currently accepted is that oxide breakdown

DOI: 10.1038/NMAT4801

arises from the generation and accumulation of defects in the oxides. There is a general consensus that a critical density of defects generated at random locations eventually leads to the formation of a localized highly conductive leakage path, or filament, across the oxide layer.

Compliance current

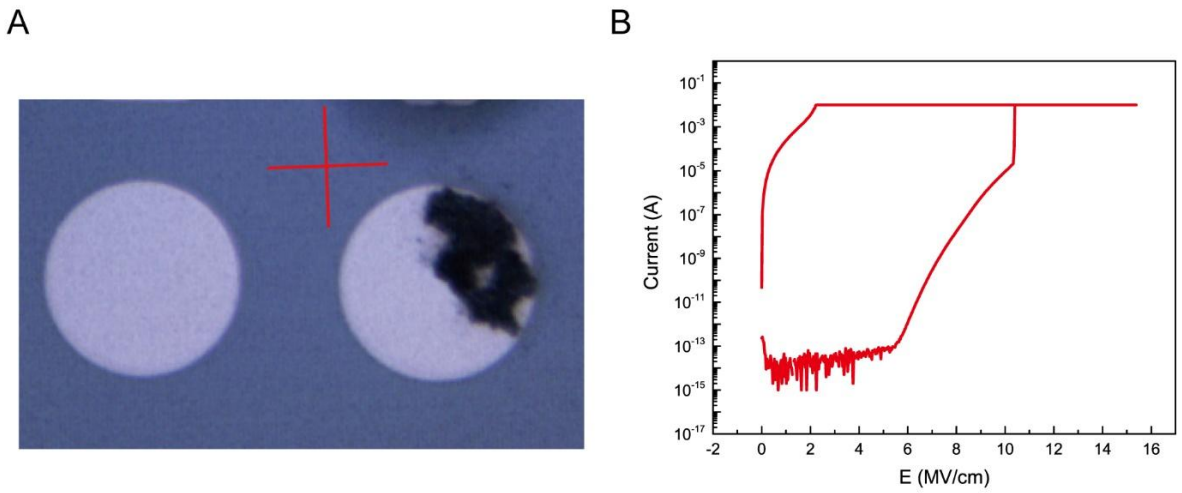

Fig. S2 (A) Optical microscope image of burned and not burned metal pad. (B) I-E characteristics of nSi/30nmSiO_2/Py devices with forward bias applied to the top metal contact (Py) with 10 mA compliance current.

In an HBD process, the high current flow after breakdown can damage or destroy the metal contact that in our work serves as a catalyst. As shown in Fig. S2(A), if no compliance current is set during voltage sweep breakdown, the total current flow across the metal pad can be so high that the metal pad is burned, as shown in the right metal dot in Fig. S2(A). Thus, a compliance current is required during the BD process to preserve the integrity of the metal catalyst. We have found that 5 mA compliance current is sufficient to protect the catalysts while providing enough current flow for the robust growth of conducting filaments. Fig. S2 (B) is a typical breakdown curve.

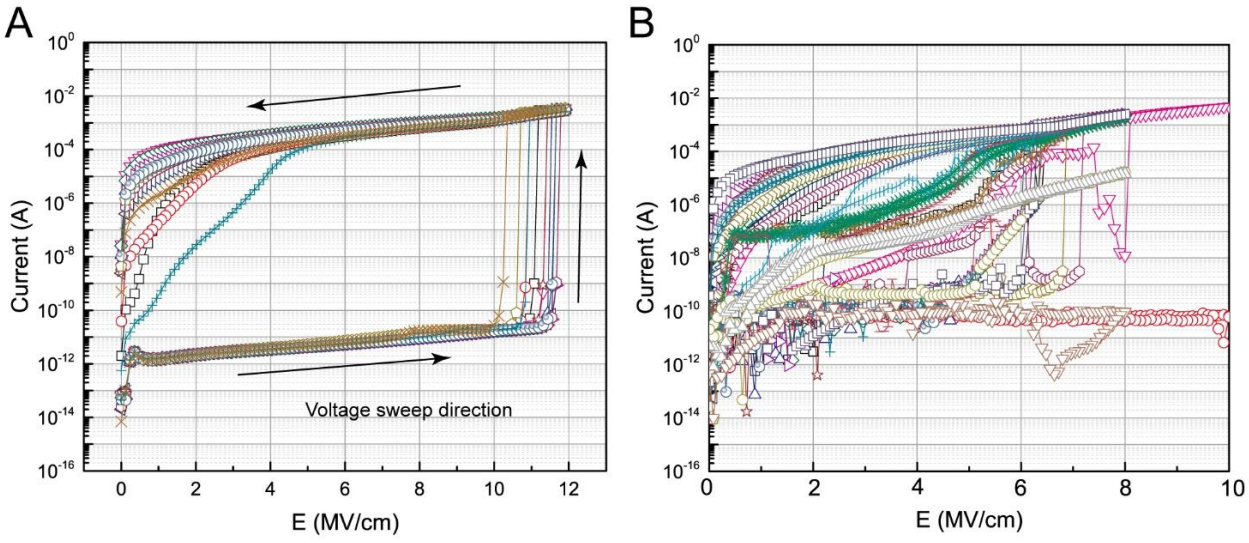

Fig. S3 Breakdown of n-Si/30nmSiO_2 samples with oxides grown by (A) thermally oxidation and (B) e-beam evaporation. The different curves in each plot represent different devices. The voltage sweep direction is as indicated as the arrows in (A)

Oxide quality effect

Since breakdown is a dynamic process, the variations from sample to sample or even device to device on the same wafer can be large. The quality of the oxide has a pronounced effect on the breakdown behavior. To study the effect of oxide quality on BD, we prepared silicon oxides by two methods, thermal oxidation, which produces low defect concentration, and e-beam evaporation, which results in much higher defect concentrations. The negative bias breakdown results are shown in Fig. S3. For thermally grown oxides, the breakdown field has a much narrower distribution than for e-beam evaporated oxides. The current levels for thermal oxides with after breakdown are overall higher that of the more defective oxides.

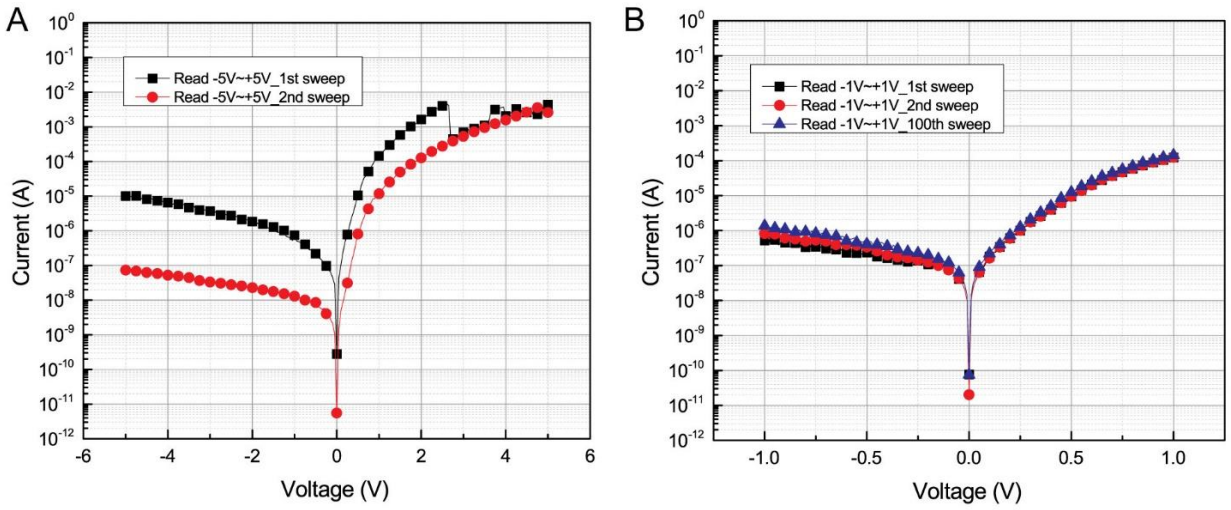

Fig. S4 I-V characteristics of nSi/30nm thermal SiO_2/Py devices after breakdown with different voltage sweep ranges, (A) -5 V ~ 5 V and (B) -1 V ~ 1V.

Read voltage range effect

After breakdown, robust device operation under extended cycling over the expected range of operating voltages is essential. Our previous work on resistive switching in intrinsic silicon oxides has shown that unipolar switching behavior occurs. Joule heating can disrupt the localized conducting path leading to a sharp decrease in electrical conduction during the reset process (*15*). As shown in Fig. S4(A), if the voltage is swept from -5 to 5 V, the power is high enough to produce joule heating and disconnect the filament, as indicated by the sharp decrease in current around 3 V. The current density is then reduced by one to two orders of magnitude when performing the 2nd sweep. If the sweep range is limited to -1 V ~ 1 V, as in Fig. S4(B), no decrease is observed after even 100 sweeps.

Metal catalyst pad size effect

DOI: 10.1038/NMAT4801

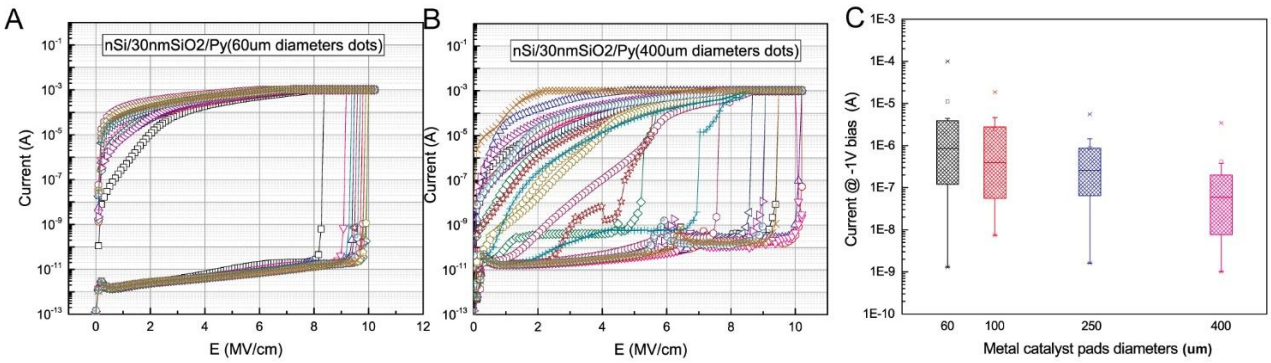

Fig. S5 Breakdown voltage sweeps of I-V characteristics for nSi/30nmSiO2/Py with (A) 60 um and (B) 400 um diameter metal contact sizes. Different curves represent different devices. (C) Statistical distribution of electrical current at -1V bias after breakdown for metal pad diameters of 60 um, 100 um, 250 um and 400 um.

The proposed filament model assumes the formation of a localized conducting path underneath metal pads, in which case conduction should be independent of the pad size. Fig. S5(A) and (B) show breakdown curves for n-Si/30nmSiO_2/Py with 60 um and 400 um diameter metal pads, respectively. There is a wide variations in BD field for 400 um diameter pads compared with those for 60 um pads, which we attribute to the increased number of defects for large pads. However, Fig. S5(C) shows that the electrical current at -1V after breakdown does not scale in proportion to the metal pad size, confirming the filament model. This results also suggests that the PEC performance can be improved by further reducing the metal catalysts sizes.

III. Permalloy ($Ni_{81}Fe_{19}$) as OER catalyst

Preparation methods

Ni based OER catalysts have been studied extensively. The first study of the effect of Fe impurities in Ni-based catalysts on OER performance was by Corrigan *et.al.* in 1988 using electrodeposited catalysts(*16*). Since then, the majority of studies have used electrodeposition to prepare NiFe or $NiFeO_x$ catalysts. Besides electrodeposition, NiFe alloys have also been prepared by mechanically mixing metallic Ni and Fe into a NiFe alloy(*17, 18*). However, this method suffered from poor film quality.

In this work, Ni (99.995%, Alfa Aesar) and $Ni_{81}Fe_{19}$ (99.95%, Alfa Aesar) films were directly deposited by e-beam evaporation (CHA Industries). The deposited thin films were polycrystalline(*19*), instead of amorphous structures prepared by mechanically mixing(*20*). The substrates were silicon wafers covered with 1600nm SiO_2. During the deposition, a vacuum was maintained with a base pressure < 2.0×10^{-6} Torr. A quartz-crystal monitor was used to monitor the deposition rates, which were kept at ~ 0.5 Å/s. The total metal film thickness for both samples was 150 nm.

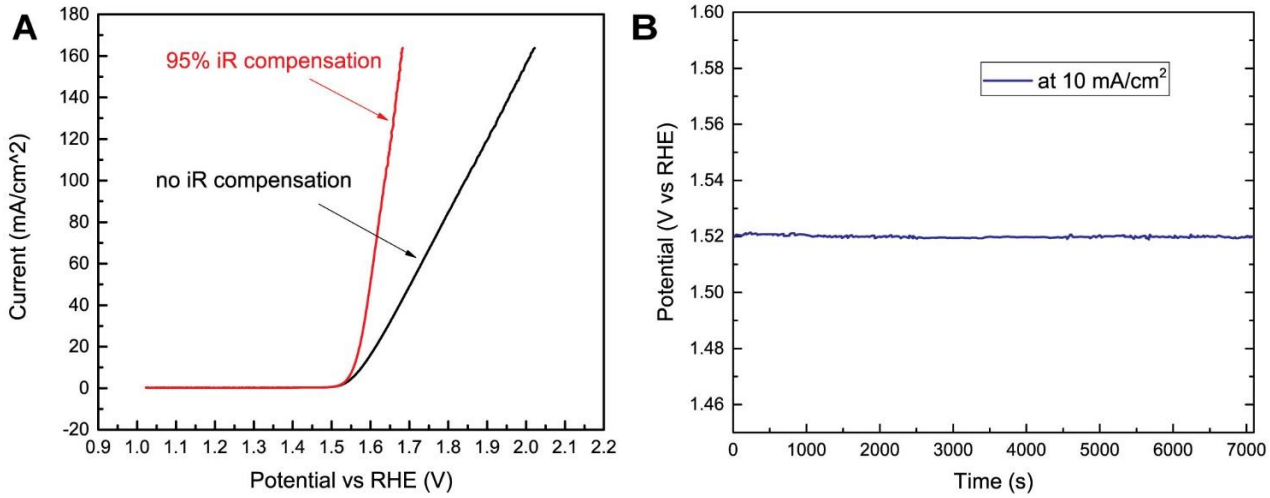

Fig. S6 (A) Linear sweep voltammetry (LSV) with and without iR-compensation, and (B) 2 h chronopotentiometry (CP) of $Ni_{81}Fe_{19}$ catalysts in 1M KOH. The scan rate for the LSV measurement was 5 mV/s and the current density for CP was at 10 mA/cm^2.

Electrochemical measurements

All electrochemical measurements were carried out with a CHI 760E electrochemical workstation (CH Instruments, Austin, United States) in a standard three-electrode electrochemical cell. A Pt wire and Ag/AgCl (3M KCL) were used as counter electrode and reference electrode, respectively. Deionized water with 18.1 MΩ resistivity was used to prepare a 1M KOH (semiconductor grade, Sigma-Aldrich, 99.99% trace metal basis) solution in which the OER characterization was carried out. All measured potentials were calibrated to RHE using the following equation:

$$E_{RHE} = E_{Ag/AgCl} + 0.197\ V + 0.059 \times pH - iR_u \qquad (1)$$

where R_u is the uncorrected resistance. The prepared electrodes were cycled ~100 times by cyclic voltammetry (CV) until stable CV curves were obtained. The electrolyte resistance was measured to be 11.1 Ω by the AC impedance method, which is a typical value for high concentration KOH solutions. Linear sweep voltammetry (LSV) of $Ni_{81}Fe_{19}$ with and without iR-compensation is shown in Fig. S6 (A). Fig. S6(B) shows a chronopotentiometry measurement of $Ni_{81}Fe_{19}$ for 2 h held at a constant current density of 10 mA/cm^2. No degradation was observed.

DOI: 10.1038/NMAT4801

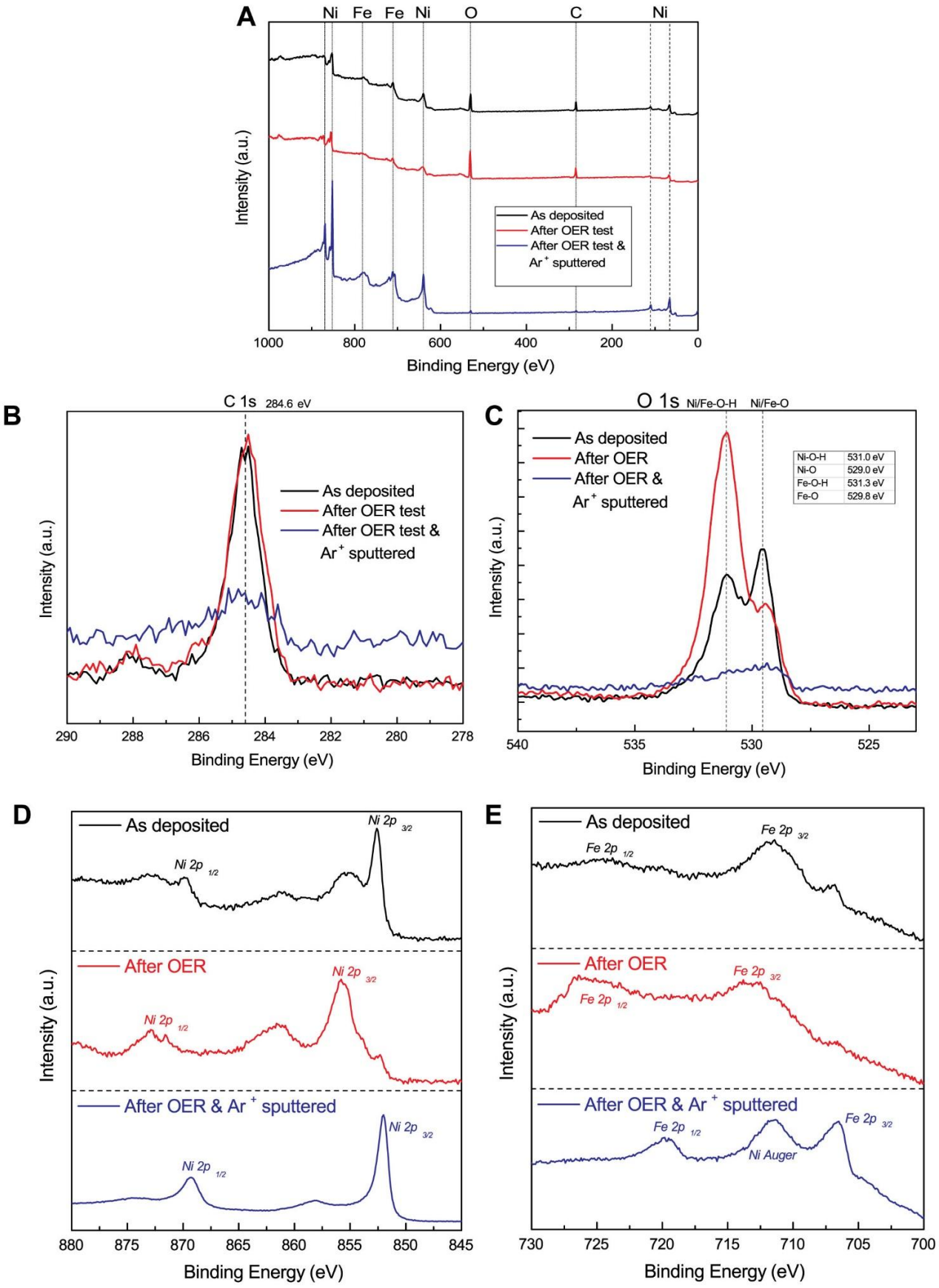

Fig. S7 XPS characterization of catalyst films (A) Survey scan, (B) C 1s and (C) O1s (D) Ni2p and (E)Fe2p high resolution scan of $Ni_{81}Fe_{19}$ catalysts under different conditions: as deposited, after OER test and after OER and 60 s Ar^+ sputtering. The sputter etch rate was approximately 0.5 nm/s. The OER test included 100 cycles CV, Tafel test and 2h chronopotentiometry at a constant current density of 10 mA/cm^2.

X-ray photoelectron spectroscopy

X-ray photoelectron spectroscopy (XPS) was performed on a Kratos Axis Ultra spectrometer XPS system. The spectra were acquired using a monochromatic Al K_α source with a base pressure of 10^{-9} Torr. Charge neutralization was used during spectrum acquisition for all measurements. A survey scan (0-1000 eV) was performed first to determine the elemental composition, as shown in Fig. S7(A), indicating the presence of Ni, Fe, O and C. High resolution spectra of the C 1s, Ni 2p, Fe 2p and O 1s peaks were then obtained with dwell times from 500-1500 ms. The C 1s peak (284.6 eV) was used for charge correction, as shown in Fig S7(B). The presence of carbon resulted from surface contamination, as ion-sputtering of the sample surface resulted in the removal of the carbon peak. The as deposited sample exhibited a mixture of Ni/Fe hydroxides and Ni/Fe oxides. After the OER test, which included cycled CV (activation process of catalysts), Tafel test and 2h chronopotentiometry, most oxide states were transformed to hydroxide states. The O 1s spectra in Fig. S7(B) also confirm the large ratio of hydroxides to oxides, which accords well with recent findings that, under potential cycling in alkaline solutions, the oxide phase slowly transforms to Ni(OH)/NiOOH, which are active sites for OER. For samples after OER test and Ar ion sputtering, the carbon and oxygen peaks are greatly reduced. This confirms that only the surface is oxidized, film is well protected, and expected to maintain high conducivity.

Supplementary Table S1 Benchmarks of OER catalysts in KOH with a current density of 10 mA/cm^2.

Materials	Electrolyte	η/mV	Reference
NiFe(permalloy)	1 M KOH	300	This work
NiFe-LDH/3D Ni foil	1 M KOH	215	Ref(*21*)
Co_3O_4/Graphene	1 M KOH	310	Ref(*22*)
$Ni_{0.9}Fe_{0.1}O_x$	1 M KOH	336	Ref(*23*)
IrO_x	0.1 M KOH	380	Ref(*24*)
RuO_x	0.1 M KOH	390	Ref(*24*)
Mn oxide	0.1 M KOH	540	Ref(*24*)
Mn_3O_4/$CoSe_2$	0.1 M KOH	450	Ref(*25*)
NiFe-LDH/CNT	1 M KOH	247	Ref(*26*)

DOI: 10.1038/NMAT4801

IV. Antireflection Functionality

Simulation methods

Numerical simulations were performed using the Rsoft Diffractmod software package (Rsoft Design Group, Inc. Ossining, NY, USA). A plane wave is used as light source perpendicular to the sample surface. The global environment was set as water to mimic the real condition of PEC measurements.

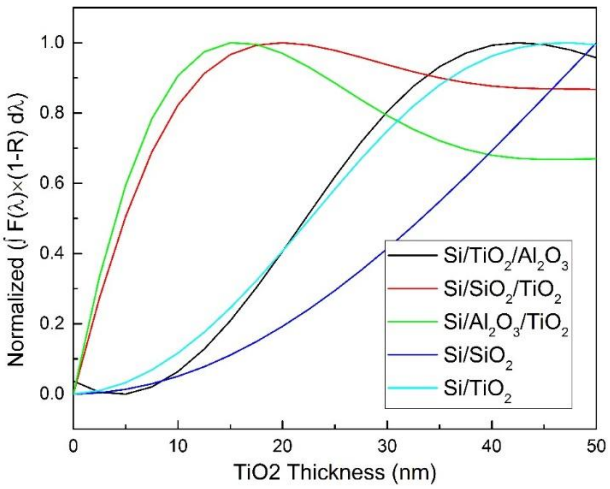

Fig. S8 Normalized integration of (1-R) over the solar spectrum. R is reflection as a function of wavelength λ. The total thickness of oxides for all samples are fixed to 50 nm, and optical obsorption in the oxide is assumed to be negligible over the wavelength range of interest.

Optimized thickness combination

The optimized thickness combination can be obtained by maximizing the optical absorption A, given by:

$$A = \int F(\lambda) \times (1 - R(\lambda)) d\lambda$$

where F(λ) is the solar spectrum and R is the reflectance. Fig. S8 shows the normalized results and the thicknesses at maximum values are the optimized thicknesses.

V. PEC characterizations

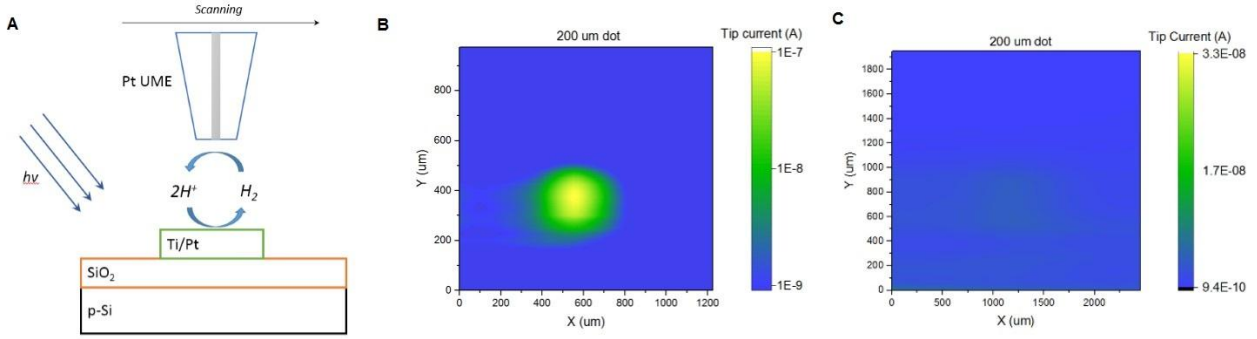

Fig S9. (A) Schematic of SECM setup. The ultramicro electrode is 10um Pt UME. Light is from side of sample and is not calibrated. (B) and (C) are SECM mappings of a 200um dot with different breakdown treatment for p-Si/30nmSiO_2/30nmTi/20nmPt sample. (B) is for device with high conductivity after breakdown and (C) is for device with low conductivity after breakdown.

Results

Fig S9 (A) is the schematic of SECM measurements. The tip of an untramicroelectrode (10um Pt UME) is positioned close to the surface of the working electrode, while its potential is held more positive than the RHE for H_2 evolution. The tip oxidation current is a measure of the rate of local H_2 evolution. To eliminate influence from adjacent dots, the metallic catalysts is patterned to 200 um diameter dots with spacing of 1600um. To avoid dramatically bubble generation on surface, which would block the tip current, a small bias is applied to the substrate. Two devices were pre-treated to present different conductivity. Device in Fig. S9 (B) has 1 mA/cm^2 current density in dry I-V measurements at 1V bias. In SECM mapping, we can see clearly the hydrogen evolution on metal pads. In comparison, device in Fig. S9 (C) has 1 uA/cm^2 current density in dry I-V measurements. And in SECM mapping, no obvious hydrogen evolution is observed.

DOI: 10.1038/NMAT4801

References

1. J. W. Lim, S. J. Yun, J. H. Lee, Low-temperature growth of SiO2 films by plasma-enhanced atomic layer deposition. *Etri J* **27**, 118-121 (2005); published online EpubFeb (

2. S. J. Won, S. Suh, M. S. Huh, H. J. Kim, High-Quality Low-Temperature Silicon Oxide by Plasma-Enhanced Atomic Layer Deposition Using a Metal-Organic Silicon Precursor and Oxygen Radical. *Ieee Electr Device L* **31**, 857-859 (2010); published online EpubAug (

3. A. Cacciato, L. Breuil, H. Dekker, M. Zahid, G. S. Kar, J. L. Everaert, G. Schoofs, X. Shi, G. Van den Bosch, M. Jurczak, I. Debusschere, J. Van Houdt, A. Cockburn, L. Date, L. Q. Xa, M. Le, W. Lee, A PEALD Tunnel Dielectric for Three-Dimensional Non-Volatile Charge-Trapping Technology. *Electrochem Solid St* **14**, H271-H273 (2011).

4. H. Profijt, S. Potts, M. Van De Sanden, W. Kessels, Plasma-assisted atomic layer deposition: basics, opportunities, and challenges. *Journal of Vacuum Science & Technology A* **29**, 050801 (2011).

5. P. Ye, G. Wilk, B. Yang, J. Kwo, S. Chu, S. Nakahara, H.-J. Gossmann, J. Mannaerts, M. Hong, K. Ng, GaAs metal–oxide–semiconductor field-effect transistor with nanometer-thin dielectric grown by atomic layer deposition. *Applied Physics Letters* **83**, 180-182 (2003).

6. X. Li, C. H. Tung, K. L. Pey, The nature of dielectric breakdown. *Applied Physics Letters* **93**, (2008); published online EpubAug 18 (

7. G. Ribes, J. Mitard, M. Denais, S. Bruyere, F. Monsieur, C. Parthasarathy, E. Vincent, G. Ghibaudo, Review on high-k dielectrics reliability issues. *Ieee T Device Mat Re* **5**, 5-19 (2005); published online EpubMar (

8. M. A. Alam, B. E. Weir, P. J. Silverman, A study of soft and hard breakdown - Part I: Analysis of statistical percolation conductance. *Ieee T Electron Dev* **49**, 232-238 (2002); published online EpubFeb (10.1109/16.981212).

9. M. A. Alam, B. E. Weir, P. J. Silverman, A study of soft and hard breakdown - Part II: Principles of area, thickness, and voltage scaling. *Ieee T Electron Dev* **49**, 239-246 (2002); published online EpubFeb (10.1109/16.981213).

10. T. Pompl, C. Engel, H. Wurzer, M. Kerber, Soft breakdown and hard breakdown in ultra-thin oxides. *Microelectron Reliab* **41**, 543-551 (2001); published online EpubApr (10.1016/s0026-2714(00)00253-5).

11. J. S. Suehle, B. Zhu, Y. Chen, J. B. Bernstein, Detailed study and projection of hard breakdown evolution in ultra-thin gate oxides. *Microelectron Reliab* **45**, 419-426 (2005); published online EpubMar-Apr (10.1016/j.microrel.2004.10.018).

12. Y. H. Kim, K. Onishi, C. S. Kang, R. Choi, H.-J. Cho, R. Nieh, J. Han, S. Krishnan, A. Shahriar, J. C. Lee, in

Electron Devices Meeting, 2002. IEDM'02. International. (IEEE, 2002), pp. 629-632.

13. Y. H. Kim, J. C. Lee, Reliability characteristics of high-k, dielectrics. *Microelectron Reliab* **44**, 183-193 (2004); published online EpubFeb (

14. E. Miranda, J. Sune, Electron transport through broken down ultra-thin SiO2 layers in MOS devices. *Microelectron Reliab* **44**, 1-23 (2004); published online EpubJan (

15. L. Ji, Y.-F. Chang, B. Fowler, Y.-C. Chen, T.-M. Tsai, K.-C. Chang, M.-C. Chen, T.-C. Chang, S. M. Sze, E. T. Yu, J. C. Lee, Integrated One Diode–One Resistor Architecture in Nanopillar SiOx Resistive Switching Memory by Nanosphere Lithography. *Nano letters* **14**, 813-818 (2014); published online Epub2014/02/12 (10.1021/nl404160u).

16. D. A. Corrigan, R. M. Bendert, Effect of coprecipitated metal ions on the electrochemistry of nickel hydroxide thin films: cyclic voltammetry in 1M KOH. *Journal of the Electrochemical Society* **136**, 723-728 (1989).

17. M. Kleinke, M. Knobel, L. Bonugli, O. Teschke, Amorphous alloys as anodic and cathodic materials for alkaline water electrolysis. *International journal of hydrogen energy* **22**, 759-762 (1997).

18. M. Plata-Torres, A. Torres-Huerta, M. Dominguez-Crespo, E. Arce-Estrada, C. Ramirez-Rodriguez, Electrochemical performance of crystalline Ni–Co–Mo–Fe electrodes obtained by mechanical alloying on the oxygen evolution reaction. *International Journal of Hydrogen Energy* **32**, 4142-4152 (2007).

19. G. C. Chi, C. J. Mogab, A. D. Burtherus, A. G. Lehner, The magnetoresistivity, structure, and magnetic anisotropy of RF sputtered and E-beam evaporated NiFe films. *Journal of Applied Physics* **52**, 2439-2441 (1981)doi:http://dx.doi.org/10.1063/1.328960).

20. M. U. Kleinke, M. Knobel, L. O. Bonugli, O. Teschke, Amorphous alloys as anodic and cathodic materials for alkaline water electrolysis. *International Journal of Hydrogen Energy* **22**, 759-762 (1997); published online Epub8// (http://dx.doi.org/10.1016/S0360-3199(96)00211-X).

21. X. Lu, C. Zhao, Electrodeposition of hierarchically structured three-dimensional nickel–iron electrodes for efficient oxygen evolution at high current densities. *Nat Commun* **6**, (2015); published online Epub03/17/online (10.1038/ncomms7616).

22. Y. Liang, Y. Li, H. Wang, J. Zhou, J. Wang, T. Regier, H. Dai, Co3O4 nanocrystals on graphene as a synergistic catalyst for oxygen reduction reaction. *Nat Mater* **10**, 780-786 (2011).

23. L. Trotochaud, J. K. Ranney, K. N. Williams, S. W. Boettcher, Solution-cast metal oxide thin film electrocatalysts for oxygen evolution. *Journal of the American Chemical Society* **134**, 17253-17261 (2012).

24. Y. Gorlin, T. F. Jaramillo, A bifunctional nonprecious metal catalyst for oxygen reduction and water oxidation.

DOI: 10.1038/NMAT4801

Journal of the American Chemical Society **132**, 13612-13614 (2010).

25. M.-R. Gao, Y.-F. Xu, J. Jiang, Y.-R. Zheng, S.-H. Yu, Water oxidation electrocatalyzed by an efficient Mn3O4/CoSe2 nanocomposite. *Journal of the American Chemical Society* **134**, 2930-2933 (2012).

26. M. Gong, Y. Li, H. Wang, Y. Liang, J. Z. Wu, J. Zhou, J. Wang, T. Regier, F. Wei, H. Dai, An Advanced Ni–Fe Layered Double Hydroxide Electrocatalyst for Water Oxidation. *Journal of the American Chemical Society* **135**, 8452-8455 (2013); published online Epub2013/06/12 (10.1021/ja4027715).